

# **Comparative pathogenicity of SARS-CoV-2 Omicron subvariants including BA.1, BA.2, and BA.5**

Tomokazu Tamura<sup>1,25</sup>, Daichi Yamasoba<sup>2,3,25</sup>, Yoshitaka Oda<sup>4,25</sup>, Jumpei Ito<sup>2,25</sup>, Tomoko Kamasaki<sup>5,6,7,25</sup>, Naganori Nao<sup>8,9,25</sup>, Rina Hashimoto<sup>10</sup>, Yoichiro Fujioka<sup>5,6,7</sup>, Rigel Suzuki<sup>1</sup>, Lei Wang<sup>4,11</sup>, Hayato Ito<sup>1</sup>, Izumi Kimura<sup>2</sup>, Isao Yokota<sup>12</sup>, Mai Kishimoto<sup>13</sup>, Masumi Tsuda<sup>4,11</sup>, Hirofumi Sawa<sup>8,9,13,14</sup>, Kumiko Yoshimatsu<sup>15</sup>, Yusuke Ohba<sup>5,6,7</sup>, Yuki Yamamoto<sup>16</sup>, Tetsuharu Nagamoto<sup>16</sup>, Jun Kanamune<sup>16</sup>, The Genotype to Phenotype Japan (G2P-Japan) Consortium, Keita Matsuno<sup>9,14,17\*</sup>, Kazuo Takayama<sup>10\*</sup>, Shinya Tanaka<sup>4,11\*</sup>, Kei Sato<sup>2,18,19,20,21,22,23\*</sup>, Takasuke Fukuhara<sup>1,24\*</sup>.

<sup>1</sup> Department of Microbiology and Immunology, Faculty of Medicine, Hokkaido University, Sapporo, Japan.

<sup>2</sup> Division of Systems Virology, Department of Microbiology and Immunology, International Research Center for Infectious Diseases, The Institute of Medical Science, The University of Tokyo, Tokyo, Japan.

<sup>3</sup> Faculty of Medicine, Kobe University, Kobe, Japan.

<sup>4</sup> Department of Cancer Pathology, Faculty of Medicine, Hokkaido University, Sapporo, Japan.

<sup>5</sup> Department of Cell Physiology, Faculty of Medicine, Hokkaido University, Sapporo, Hokkaido, Japan.

<sup>6</sup> Global Station for Biosurfaces and Drug Discovery, Hokkaido University, Sapporo, Hokkaido, Japan.

<sup>7</sup> AMED-CREST, Japan Agency for Medical Research and Development, Sapporo, Hokkaido, Japan.

<sup>8</sup> Division of International Research Promotion, International Institute for Zoonosis Control, Hokkaido University, Sapporo, Japan.

<sup>9</sup> One Health Research Center, Hokkaido University, Sapporo, Japan.

<sup>10</sup> Center for iPS Cell Research and Application (CiRA), Kyoto University, Kyoto, Japan.

<sup>11</sup> Institute for Chemical Reaction Design and Discovery (WPI-ICReDD), Hokkaido University, Sapporo, Japan.

<sup>12</sup> Department of Biostatistics, Faculty of Medicine, Hokkaido University, Sapporo, Japan.

<sup>13</sup> Division of Molecular Pathobiology, International Institute for Zoonosis Control, Hokkaido University, Sapporo, Japan.

<sup>14</sup> International Collaboration Unit, International Institute for Zoonosis Control, Hokkaido University, Sapporo, Japan.

<sup>15</sup> Institute for Genetic Medicine, Hokkaido University, Sapporo, Japan.

<sup>16</sup> HiLung Inc., Kyoto, Japan

42 <sup>17</sup> Division of Risk Analysis and Management, International Institute for Zoonosis  
43 Control, Hokkaido University, Sapporo, Japan.

44 <sup>18</sup> Graduate School of Medicine, The University of Tokyo, Tokyo, Japan.

45 <sup>19</sup> Graduate School of Frontier Sciences, The University of Tokyo, Kashiwa,  
46 Chiba, Japan

47 <sup>20</sup> International Research Center for Infectious Diseases, The Institute of Medical  
48 Science, The University of Tokyo, Tokyo, Japan

49 <sup>21</sup> International Vaccine Design Center, The Institute of Medical Science, The  
50 University of Tokyo, Tokyo, Japan

51 <sup>22</sup> Collaboration Unit for Infection, Joint Research Center for Human Retrovirus  
52 infection, Kumamoto University, Kumamoto, Japan.

53 <sup>23</sup> CREST, Japan Science and Technology Agency, Kawaguchi, Japan.

54 <sup>24</sup> Laboratory of Virus Control, Research Institute for Microbial Diseases, Osaka  
55 University, Suita, Japan.

56 <sup>25</sup> These authors contributed equally

57

58 \*Corresponding authors:

59 matsuk@czc.hokudai.ac.jp (Keita Matsuno),

60 kazuo.takayama@cira.kyoto-u.ac.jp (Kazuo Takayama)

61 tanaka@med.hokudai.ac.jp (Shinya Tanaka),

62 KeiSato@g.ecc.u-tokyo.ac.jp (Kei Sato),

63 fukut@pop.med.hokudai.ac.jp (Takasuke Fukuhara)

64

65 **Keywords:**

66 SARS-CoV-2; COVID-19; BA.1; BA.2; BA.5; pathogenicity

67

68 **Conflict of interest:**

69 Yuki Yamamoto and Tetsuharu Nagamoto are founders and shareholders of

70 HiLung, Inc. Jun Kanamune is an employee of HiLung, Inc. Yuki Yamamoto is a

71 co-inventor of patents (PCT/JP2016/057254; "Method for inducing differentiation

72 of alveolar epithelial cells", PCT/JP2016/059786, "Method of producing airway

73 epithelial cells"). The other authors declare that no competing interests exist.

74

## 75 **Abstract**

76 Unremitting emergence of severe acute respiratory syndrome coronavirus 2  
 77 (SARS-CoV-2) variants imposes us to continuous control measurement. Given  
 78 the rapid spread, new Omicron subvariant named BA.5 is urgently required for  
 79 characterization. Here we analyzed BA.5 with the other Omicron variants BA.1,  
 80 BA.2, and ancestral B.1.1 comprehensively. Although *in vitro* growth kinetics of  
 81 BA.5 is comparable among the Omicron subvariants, BA.5 become much more  
 82 fusogenic than BA.1 and BA.2. The airway-on-a-chip analysis showed that the  
 83 ability of BA.5 to disrupt the respiratory epithelial and endothelial barriers is  
 84 enhanced among Omicron subvariants. Furthermore, in our hamster model, *in*  
 85 *vivo* replication of BA.5 is comparable with that of the other Omicrons and less  
 86 than that of the ancestral B.1.1. Importantly, inflammatory response against  
 87 BA.5 is strong compared with BA.1 and BA.2. Our data suggest that BA.5 is still  
 88 low pathogenic compared to ancestral strain but evolved to induce enhanced  
 89 inflammation when compared to prior Omicron subvariants.

## 90 **Main**

91 In recent months, multiple omicron sub-lineages of severe acute respiratory  
 92 syndrome coronavirus 2 (SARS-CoV-2) have emerged<sup>1</sup> and impose continually  
 93 public concerns for COVID-19 control measurement. The subvariants named  
 94 BA.4/BA.5 are firstly isolated in South Africa<sup>2</sup>. Now they have been detected in  
 95 dozens of countries worldwide, with a combined frequency of over 50% in recent  
 96 weeks at the time of writing the initial manuscript of this study in July 2022. As of  
 97 August 2022, BA.5 has outcompeted the original BA.2 and becomes dominant  
 98 variant in the world. The raising cases of COVID-19 by BA.4/BA.5 indicate that  
 99 they acquire the enhanced transmission ability compared to the sister lineages,  
 100 BA.1 and BA.2. Indeed, as shown in a recent report from Portugal where  
 101 outbreak by BA.5 was occurred<sup>3</sup>, morbidity of BA.5 is higher than that of BA.1  
 102 variants. To answer potential urgency for COVID-19 wave, the several groups  
 103 conducted the ability of immunoprophylaxis conferred by vaccination or infection  
 104 with previous variants. The recent reports showed that BA.4/BA.5 substantially  
 105 escape from neutralizing antibodies induced by vaccination or infection<sup>4-8</sup>. By  
 106 genome sequencing and evolutionary analyses, BA.4 and BA.5 are more similar  
 107 to BA.2 than to the BA.1 strain that surged in late last year. We have been  
 108 shown that viral spike protein is one of the major virulence determinants<sup>9-12</sup>.  
 109 BA.4 and BA.5 have identical spike protein and carry their own unique mutations,  
 110 including L452R that exhibited the enhanced fusogenic activity and pose  
 111 resistant to the immunity induced by the infection with early variants<sup>13</sup>. This  
 112 observation is consistent with the series of our studies using the recombinant  
 113 viruses replacing the spike protein gene from the ancestral early pandemic  
 114 variants. However, virological characters of BA.5 strain isolated from COVID-19  
 115 patients has not yet fully defined. Here, we employed the indicated omicron  
 116 subvariants (BA.1 lineage, strain TY38-873, GISAID ID: EPI\_ISL\_7418017;  
 117 BA.2 lineage, strain TY40-385, GISAID ID: EPI\_ISL\_9595859; BA.5 lineage,  
 118 strain TKYS14631, GISAID ID: EPI\_ISL\_12812500)<sup>14</sup> for investigating  
 119 virological characters *in vitro* and *in vivo* model.

## 121 **Virological features of Omicron subvariants *in vitro***

122 To elucidate the virological characteristics of Omicron subvariants, we obtained  
 123 BA.1 isolate (strain TY38-873), BA.2 isolate (strain TY40-385), and BA.5 isolate  
 124 (strain TKYS14631). A D614G-bearing early pandemic B.1.1 isolate (strain  
 125 TKYE610670)<sup>10</sup> was used as a control. Then we characterized their *in vitro*  
 126 growth kinetics using the cell lines VeroE6/TMPRSS2<sup>15</sup>, Calu-3, and iPS  
 127 cell-derived alveolar epithelial cells (**Fig. 1A, B**). In the cell lines  
 128 VeroE6/TMPRSS2 and Calu-3, BA.2 and BA.5 subvariants are comparable  
 129 replication to the B.1.1 but BA.1 showed low replication rate. In the iPS  
 130 cell-derived alveolar epithelium cells, B.1.1, BA.1, and BA.5 exhibited the slightly

high replication efficiency compared with the strain BA.2, suggesting that the replication property of Omicron subvariant BA.5 *in vitro* is similar to that of B.1.1. Although the growth kinetics of Omicron subvariants and B.1.1 in VeroE6/TMPRSS2 cells were comparable (**Fig. 1A**), the morphology of infected cells was quite different; B.1.1 formed larger syncytia than the Omicron subvariants (**Fig. 1C**). To further investigate syncytia formation of the Omicron subvariants, we generated the VeroE6/TMPRSS2 cells expressing either EGFP or mCherry and an equal amount of them were seeded for syncytia formation as a merged image (**Fig. 1D**). Within Omicron subvariants, the ability of syncytia formation of BA.1 is lower than that of BA.2 and BA.5. Consistent with observation of syncytia, efficacy of cleavage of S protein by B.1.1 infection was highest of all (**Fig. 1E**). Among the Omicron subvariants, BA.5 exhibited most efficient activity of S cleavage. These data suggest that even though Omicron subvariants are still less fusogenic than B.1.1 isolate, the subvariants are evolving toward efficient fusogenicity in VeroE6/TMPRSS2 cells. A previous study has shown that some ultrastructural changes are detected in SARS-CoV-2-infected cells at early phase of post infection<sup>16</sup>. One of the alterations is the presence of annulate lamellae (AL) in the cell sections. AL are characterized as stacks of ER-derived membranes highly arranged in parallel and containing nuclear pore complexes<sup>17</sup>. To investigate whether the difference in the extent of AL formation upon infection with the variants, we performed electron microscopic analysis (**Fig. 1F**) of SARS-CoV-2-infected VeroE6/TMPRSS2 cells at early phase of post infection (multiplicity of infection, m.o.i. = 0.01, 16 h.p.i). In uninfected cells, AL were not seen even at late phase (32 h.p.i) (**Fig. 1F**: mock). In contrast, by virus infection, several membranous structures (~80 nm) were gathered within electron-dense areas near the nucleus (**Fig. 1F**: B.1.1, BA.1, BA.2) or at the expansion of the nuclear envelope (**Fig. 1F**: BA.5). They exhibited ultrastructural resemblance to cross sections of AL as shown in the earlier report<sup>16</sup>, suggesting that B.1.1 and Omicron subvariants are similar replication rate at the earlier stage of virus life cycle. Next, to evaluate the influence of viral infection on the respiratory epithelial and endothelial barriers, airway-on-a-chip was utilized; by examining the amount of virus that migrates from the airway channel to the blood vessel channel, the ability to disrupt the respiratory epithelial and endothelial barriers can be evaluated. In the Omicron subvariants, the largest amount of virus was detected in the blood vessel channel of BA.5-infected airway-on-a-chip. In addition, the B.1.1- and BA.5-infected airway-on-chip exhibited more severe disruption than the BA.1- and BA.2-infected ones, suggesting that BA.5 possesses a substantial barrier disruption capacity (**Fig. 1G**).

172

### 173 **Virological features of Omicron subvariants *in vivo***

174 To investigate the dynamics of viral replication *in vivo* and pathogenicity of  
 175 Omicron subvariants, we utilized the established animal model using hamsters  
 176 <sup>9-11</sup>. Consistent with our previous study, B.1.1-infected hamsters exhibited  
 177 decreased body weight from day 2 post-infection (p.i.) (**Fig. 2A**). The change of  
 178 the body weight of Omicron subvariants-infected hamsters was moderate  
 179 compared with that of B.1.1-infected hamsters and similar to the uninfected  
 180 group. Importantly, the dynamics of weight changes of BA.5-infected hamsters  
 181 was significantly different from that of the BA.2-infected and uninfected hamsters  
 182 (**Fig. 2A**). We then quantitatively analyzed the pulmonary function of infected  
 183 hamsters as reflected by three parameters, namely, enhanced pause (Penh)  
 184 and the ratio of time to peak expiratory flow relative to the total expiratory time  
 185 (Rpef), which are surrogate markers for bronchoconstriction or airway  
 186 obstruction, and subcutaneous oxygen saturation (SpO<sub>2</sub>). As shown in **Fig.**  
 187 **2B–D**, the B.1.1-infected hamsters exhibited respiratory disorders according to  
 188 these three parameters. In contrast, in BA.1-, BA.2- and BA.5-infected hamsters,  
 189 the Penh value was significantly lower than those in B.1.1-infected hamsters  
 190 (**Fig. 2B**), and the Rpef value was significantly higher than those in  
 191 B.1.1-infected hamsters (**Fig. 2C**). As per SpO<sub>2</sub> values, B.1.1- and BA.5-infected  
 192 hamsters exhibited lower tendency than those of BA.1- and BA.2-infected  
 193 hamsters (**Fig. 2D**). *In vivo* viral dynamics was analyzed by collecting the oral  
 194 swab of infected hamsters at indicated timepoints (**Fig. 2E**). On day 1 p.i., the  
 195 viral loads of Omicron subvariants-infected hamsters were significantly lower  
 196 than those of B.1.1-infected hamsters. These data suggest that Omicron  
 197 subvariants are less pathogenic than the B.1.1, but BA.5 is evolving toward  
 198 slightly increased pathogenicity.

199 We next assessed viral spreading in the respiratory tissues and, thus, collected  
 200 the trachea and the lung on day 2 and 5 p.i. (**Fig. 3A**). In the upper trachea of  
 201 infected hamsters, epithelial cells were sporadically positive for viral N protein on  
 202 day 2 p.i., but there were no significant differences among B.1.1 and Omicron  
 203 subvariants (**Fig. S1B**). As per lung, we investigated the viral spreading in the  
 204 separate region, hilum and periphery. In the lung hilum, although viral RNA  
 205 copies (**Fig. 3A**, left) in the lung hilum of BA.1 were approximately 10-fold lower  
 206 than those of B.1.1, BA.2, and BA.5 on day 2 p.i., viral RNAs of all omicron  
 207 subvariants were significantly lower than those of B.1.1 on day 5 p.i. In contrast  
 208 to the hilum, viral RNA copies (**Fig. 3A**, middle) and titers (**Fig. 3A**, right) in the  
 209 periphery was slightly different among Omicron subvariants. Large amounts of  
 210 viral load were detected from BA.5 on day 2 p.i. that is comparable to B.1.1. To  
 211 further characterize virus spread by Omicron subvariants, immunohistochemical  
 212 (IHC) analysis of viral N protein was conducted using the specimens of



respiratory system. On day 2 p.i., the N protein was observed in the alveolar space around the bronchi/bronchioles in the B.1.1-infected hamsters (**Fig. 3B**, top panel). In Omicron BA.2- and BA.5-infected hamsters, the N protein was observed in the alveolar space with less extent than those of B.1.1. The N proteins strongly remain in lobar bronchi in the BA.5-, but not BA.2-, infected hamsters (**Fig. 3B**, BA.5: bottom panel, BA.2: third panel). In contrast, few N protein was detected in the BA.1-infected lungs (**Fig. 3B**, second top panel). On day 5 p.i., B.1.1- and BA.5 N proteins were also distributed in the peripheral alveolar space and the higher amount was observed in the group of B.1.1 (**Fig. 3B**). The N proteins were hardly detected in the lungs infected with BA.1 and BA.2. These data suggest that BA.5 efficiently infect bronchial/bronchiolar epithelium and invade the alveolar space more than BA.1 and BA.2. In contrast, BA.1 and BA.2 infect only a portion of bronchial/bronchiolar epithelium and is less efficiently transmitted to the neighboring epithelial cells. Overall, IHC data suggest that BA.5 has a higher spread of infection from the bronchi/bronchioles to the peripheral part of the alveoli than BA.1 and BA.2 but not reaches to the levels of B.1.1.

### **Inflammation in lung tissue infected with Omicron subvariants**

To further investigate the pathogenicity of Omicron subvariants in the lung, the formalin-fixed right lungs of infected hamsters were analyzed by carefully identifying the four lobules and main bronchus and lobar bronchi sectioning each lobe along with the bronchial branches. Histopathological scoring was performed as described in the previous study<sup>9-11</sup>. Briefly, pathological features including bronchitis or bronchiolitis, hemorrhage or congestion, alveolar damage with epithelial apoptosis and macrophage infiltration, and hyperplasia of type II pneumocytes were evaluated by certified pathologists and the degree of these pathological findings were arbitrarily scored using four-tiered system as 0 (negative), 1 (weak), 2 (moderate), and 3 (severe). Bronchitis is an inflammatory indicator at early stage of infection. On day 2 p.i., the B.1.1-infected hamsters showed most severe bronchiolitis followed by BA.5-, BA.2-, and BA.1-infected hamsters (**Fig. 4A, B**). On day 5 p.i., the B.1.1-infected hamsters exhibited more severe alveolar damage, hemorrhage, and type II pneumocytes than the animals infected with Omicron variants (**Fig. 4A, 4B**). Between BA.5 and the parental BA.2, infection with BA.5 exhibited more severe inflammation including the alveolar damage as infiltration of lymphocytes and macrophages (score 2.0) and the presence of type II pneumocytes with enlarged cellular cytoplasm and nucleus (score 2.0) compared with BA.2 (both scores 1.75). Higher degree of hemorrhage was observed in BA.5 (2.5) than BA.2 (2.25) (**Fig. 4A**). In case of BA.1-infection, all histological scores were lowest on day 5 p.i. (**Fig. 4A**). Although B.1.1 infection caused most severe inflammation, these data suggest

254 that BA.5 inflammation caused severe inflammation among Omicron  
255 subvariants.

256 Because the difference of histological scoring among the Omicron subvariants  
257 were little, inflammatory area mainly composed of the type II pneumocytes with  
258 various inflammatory cells as neutrophils, lymphocytes, and macrophages  
259 (termed the area of type II pneumocytes) were morphometrically analyzed and  
260 found that the area of type II pneumocytes was significantly higher in BA.5  
261 (50.5%) than BA.1 (27.2%) or BA.2 (30.2%) (**Fig. 4C** and **Supplementary Fig.**  
262 **4**), suggesting that deterioration of inflammation might determine increased  
263 pathogenicity of BA.5 in hamsters. Thus, we evaluated inflammatory response  
264 upon infection with Omicron subvariants *in vivo*, the mRNA of the lung hilum  
265 area on day 2 p.i. and 4 parameters (*CXCL10*, *IL-6*, *ISG15*, and *MX-1*) were  
266 measured (**Fig. 4D**). Upon infection with all variants, the evaluated ISGs,  
267 *CXCL10*, *ISG15*, and *MX-1*, were upregulated and the expression levels by  
268 B.1.1 were highest then followed by the BA.5. The expression of *IL-6* was also  
269 upregulated and was remained only of B.1.1-infected hamsters but not of  
270 Omicron subvariants-infected ones, suggesting that anti-viral inflammatory  
271 response led to deterioration of pathogenicity.

272

## 273 Discussion

274 Because a new subvariants BA.5 is surged dramatically and outcompeted to the  
275 parental BA.1 and BA.2 variants, researchers rapidly dispatched reports  
276 showing further resistance of the SARS-CoV-2 Omicron variant against the  
277 immunity elicited by previous infections and vaccination<sup>18-23</sup>. In addition, the  
278 morbidity of COVID-19 by infection with BA.5 is escalated<sup>3</sup>, suggesting that the  
279 appropriate implementation of control measurement is urgently required.  
280 However, comparative analysis of these Omicron subvariants, BA.1, BA.2, and  
281 BA.5 have not been well documented. Kawaoka et al. showed that the clinical  
282 isolate BA.5 exhibited lower pathogenicity than the ancestral Delta in hamster  
283 models<sup>24</sup>. We recently reported that the spike protein of BA.5 contributes the  
284 enhanced pathogenicity compared to the previous Omicron subvariant BA.2 in  
285 our hamster model. Here, we further investigate the *in vitro* and *in vivo*  
286 characters of three clinical isolates of Omicron subvariants BA.1, BA.2, and BA.5.  
287 Although the virulence of the Omicron subvariants is less than that of the  
288 ancestral lineage B.1.1, our comprehensive analyses suggest that the BA.5  
289 gains pathogenicity by evolving to enhance inflammatory response. This might  
290 be a key factor for deterioration of mobility in human population by BA.5  
291 infection<sup>3</sup>.

292 As we showed the series of studies using the recombinant viruses<sup>9-12</sup>,  
293 fusogenicity by the viral spike protein has a great impact on viral replication and  
294 pathogenesis. Consistent with these, the fusogenicity of the Omicron



subvariants were less than the conventional B.1.1 strain and BA.5 exhibited slight high fusogenicity among Omicron subvariants (**Figs. 1C, 1D and 1E**). In addition, *in vitro* growth kinetics is similar in cell lines, VeroE6/TMPRSS2, Calu-3 cells and in iPS cell-derived lung epithelial cells (**Figs. 1A and 1B**). Interestingly however, investigation with airway-on-a-chip as much more mimic *in vivo* environment were conducted and the resulting data showed that BA.5 has a strong barrier disruption capacity among the Omicron subvariants (**Fig. 1F**). In the hamsters, infection with BA.5 showed the strong hemorrhage and alveolar damage (**Figs. 4A and 4B**), supporting the enhanced phenotype of BA.5 for invasion of respiratory tissues.

Kawaoka et al. recently showed that the Omicron subvariants including BA.5 is less pathogenic than Delta and deterioration of weight loss by BA.5 infection is slightly higher than that by BA.2 infection. In the present study, the weight loss in BA.5 infected hamsters was higher than that of other Omicron subvariants, consisting with this. In addition, by using the recombinant virus replacing spike protein gene with the BA.2 backbone, the recombinant virus bearing BA.4/5 spike protein exhibited significantly enhanced pathogenicity in hamsters in our previous study. In combination with our present and previous studies, the possible evolution of BA.5 spike protein to achieve higher pathogenicity shall need to be underscored.

Of these Omicron subvariants, BA.5 exhibited deterioration of weight loss and of respiratory markers (**Fig. 2**). BA.5 isolate efficiently infect bronchial/bronchiolar epithelium and invade the alveolar space leading to the remaining virus replication in the lung. As shown in a clinical report, BA.5 exhibits higher morbidity than BA.2, suggesting inflammation influences outcoming clinical manifestations. Thus, we evaluated the inflammatory responses evoked by viral infection. By morphometrical analysis which is sensitive to reflect the subtle difference of inflammations, the inflammatory area of the lungs infected with BA.5 was larger than that of BA.2 and approximately equal to B.1.1. on day 5 p.i. (**Fig. 4C**), indicating that BA.5 is more immunopathogenic than BA.2. In mRNA levels, interferon-stimulating genes including *CXCL10*, *ISG15*, and *MX-1* were upregulated upon infection (**Fig. 4D**). Reuschl et al., showed the enhanced innate immune suppression by BA.4 and BA.5 compared with the previous BA.2 subvariants<sup>25</sup>. Altogether, severe inflammations of BA.5 might reflect severe clinical manifestations currently happening in human population<sup>3</sup>.

In summary, our analyses using clinically isolated Omicron subvariants, BA.1, BA.2, and BA.5 by *in vitro* experiments and the established animal models contributed to improved understanding of SARS-CoV-2 ecology and evolution. Our findings suggest that the characterization described herein should be offered as an aid in implementing control measurements on COVID-19.

## 336 **Figure legends**

### 337 **Fig. 1 | Virological features of Omicron subvariants *in vitro*.**

338 **A,B**, Growth kinetics of Omicron subvariants. The four clinical isolates of B.1.1,  
339 Omicron BA.1, BA.2, and BA.5 were inoculated into VeroE6/TMPRSS2, Calu-3  
340 (**A**) and human alveolar epithelial (**B**) cells, and the copy number of the viral  
341 RNA in the supernatant was quantified by RT-qPCR. **C**, Bright-field images of  
342 infected VeroE6/TMPRSS2 cells (m.o.i. = 0.01) at 48 h.p.i. SARS-CoV-2  
343 induced syncytia formation. EGFP- and mCherry-expressing VeroE6/TMPRSS2  
344 cells were co-cultured at a 1:1 ratio and infected with B.1.1, BA.1, BA.2, and  
345 BA.5 isolates. Scale bars, 200  $\mu$ m **D**. Syncytia formation was monitored by  
346 immunofluorescent microscopy at 48 h.p.i. Scale bars, 100  $\mu$ m. **E**, Expressions  
347 of S protein (S1+S2 and S2) were examined by immunoblotting by monoclonal  
348 antibody against S upon infection with the respective SARS-CoV-2 variants in  
349 the VeroE6/TMPRSS2 cells. **F**, Ultrastructure of annulate lamellae (AL) in  
350 SARS-CoV-2 infected cells at 16 h.p.i. Arrowhead represents the membranous  
351 lamella which constitutes AL. Scale bar, 0.5  $\mu$ m. **F**, The efficiency of S cleavage  
352 is evaluated by immunoblotting analysis. **G**, Airway-on-a-chip analysis. Medium  
353 containing SARS-CoV-2 was injected into the airway channel, which was then  
354 cultured for 6 days. Viral RNA in the supernatant of both the airway and blood  
355 vessel channels were quantified by RT-qPCR. Data are the average  $\pm$  s.d. The  
356 ratio of viral invasion toward blood vessel channels were calculated (blood  
357 vessel channel/airway channel) on day 6 p.i. as shown percentages. (**A,B,G**).  
358 Assays were performed independently in two-time (**A**) or triplicate (**B,G**). In **G**,  
359 statistically significant differences between B1.1 and other variants ( $\ddagger$ ,  $P < 0.05$ ),  
360 and between BA.5 and other variants (\*,  $P < 0.05$ ) were determined by two-sided  
361 Student's *t* tests.

### 363 **Fig. 2 | Time-course dynamics of Omicron subvariants *in vivo*.**

364 Syrian hamsters were intranasally inoculated with saline ( $n = 6$ , uninfected  
365 control), B.1.1 ( $n = 6$ ), BA.1 ( $n = 6$ ), BA.2 ( $n = 6$ ) and BA.5 ( $n = 6$ ). Body weight  
366 (**A**), Penh (**B**), Rpef (**C**), SpO<sub>2</sub> (**D**), and viral RNA load in the oral swab (**E**) were  
367 routinely measured as indicated in the graph. Data are the average  $\pm$  s.e.m. In **A**,  
368 statistically significant differences between BA.5 and other variants or saline  
369 across timepoints from on day 1 p.i. to on day 7 p.i. were determined by multiple  
370 regression (\*,  $P < 0.05$ ). The family-wise error rates calculated using the Holm  
371 method are indicated in the figure. In **B-D**, statically differences B.1.1 and other  
372 variants or saline were tested with Tukey's multiplicity correction ( $\ddagger$ ,  $P < 0.05$ ).  
373 Statically differences BA.5 and other variants or saline were tested with Tukey's  
374 multiplicity correction (\*,  $P < 0.05$ ).

377

378 **Fig. 3 | Virological features of Omicron subvariants *in vivo*.**

379 Syrian hamsters were intranasally inoculated with B.1.1 ( $n = 4$ ), BA.1 ( $n = 4$ ),  
380 BA.2 ( $n = 4$ ), and BA.5 ( $n = 4$ ). (A) Viral RNA quantification and titration. Viral  
381 RNA load (left, middle) in the lung hilum and periphery and viral titer (right) in the  
382 lung periphery were quantified. Statically differences between B.1.1 and other  
383 variants were tested with Tukey's multiplicity correction ( $\ddagger$ ,  $P < 0.05$ ) and  
384 differences between B.1.1 and other variants (\*,  $P < 0.05$ ).

385 (B) IHC of the SARS-CoV-2 N protein in the lungs of infected hamsters.  
386 Representative IHC panels of the viral N proteins in the lower lobe of lungs of the  
387 infected hamsters. Scale bars, 500  $\mu$ m.

388

389 **Fig. 4 | Pathological features of Omicron subvariants.**

390 Syrian hamsters were intranasally inoculated with B.1.1 ( $n = 4$ ), BA.1 ( $n = 4$ ),  
391 BA.2 ( $n = 4$ ) and BA.5 ( $n = 4$ ). (A) Histopathological scoring of lung lesions. (B)  
392 H&E staining of the lungs of infected hamsters. Uninfected lung alveolar space  
393 and bronchioles are also shown. (C) Summary of the percentage of the section  
394 represented by the inflammatory area with type II pneumocytes. The raw data  
395 are shown in **Figure S4**. (D) mRNA of the lung tissues obtained on day 2 post  
396 infection were used to measure expression levels of inflammatory genes  
397 (*CXCL10*, *IL-6*, *ISG15*, and *MX-1*) with normalization of a house-keeping gene,  
398 RPL18. In C, data are the average  $\pm$  S.E.M. In A, C, and D, each dot indicates  
399 the result from an individual hamster. In C, statistically significant differences (\*,  
400  $P < 0.05$ ) were determined by two-sided unpaired Student's *t*-tests without  
401 adjustment for multiple comparisons. In D, differences among Omicron  
402 subvariants were tested with Tukey's multiplicity correction (\*,  $P < 0.05$ ).

403

## 404 **Methods**

### 405 **Ethics statement**

406 All experiments with hamsters were performed in accordance with the Science  
407 Council of Japan's Guidelines for the Proper Conduct of Animal Experiments.  
408 The protocols were approved by the Institutional Animal Care and Use  
409 Committee of National University Corporation Hokkaido University (approval  
410 numbers 20-0123 and 20-0060).

411

### 412 **Cell culture**

413 HEK293-ACE2/TMPRSS2 cells [HEK293 cells (ATCC CRL-1573) stably  
414 expressing human ACE2 and TMPRSS2]<sup>12</sup> were maintained in Dulbecco's  
415 modified Eagle's medium (DMEM) (high glucose) (Nacalai Tesque, Cat#  
416 08459-64) containing 10% fetal bovine serum (FBS) and 1%  
417 penicillin-streptomycin (PS). VeroE6/TMPRSS2 cells (VeroE6 cells stably  
418 expressing human TMPRSS2; JCRB1819)<sup>15</sup> were maintained in DMEM (low  
419 glucose) (Sigma-aldrich, Cat# D6046-500ML) containing 10% FBS, G418 (1  
420 mg/ml; Nacalai Tesque, Cat# G8168-10ML) and 1% PS. Calu-3 cells (a human  
421 airway epithelial cell; ATCC HTB-55) were maintained in EMEM (Wako, Cat#  
422 055-08975) containing 10% FBS and 1% PS. Human alveolar epithelial cells  
423 derived from human induced pluripotent stem cells (iPSCs) were manufactured  
424 according to established protocols as described below (see "Preparation of  
425 human alveolar epithelial cells from human iPSCs" section) and provided by  
426 HiLung Inc.

427

### 428 **Preparation of human alveolar epithelial cells from human iPSCs**

429 The air-liquid interface culture of alveolar epithelial cells were differentiated from  
430 human iPSC-derived lung progenitor cells as previously described<sup>26-28</sup>. Briefly,  
431 lung progenitor cells were stepwise induced from human iPSCs referring a  
432 21-days and 4-steps protocol<sup>26</sup>. On day 21, lung progenitor cells were isolated  
433 with specific surface antigen carboxypeptidase M and seeded onto upper  
434 chamber of 24-well Cell Culture Insert (Falcon, #353104), followed by 28-day  
435 and 7-day differentiation of alveolar epithelial cells, respectively. Alveolar  
436 differentiation medium supplemented with dexamethasone (Sigma-Aldrich, Cat#  
437 D4902), KGF (PeproTech, Cat# 100-19), 8-Br-cAMP (Biolog, Cat# B007),  
438 3-Isobutyl 1-methylxanthine (IBMX), CHIR99021 (Axon Medchem, Cat# 1386),  
439 and SB431542 (FUJIFILM Wako, Cat# 198-16543) was used for induction of  
440 alveolar epithelial cells. PneumaCult ALI (STEMCELL Technologies, Cat#  
441 ST-05001) supplemented with heparin and Y-27632 (LC Laboratories, Cat#  
442 Y-5301) hydrocortisone (Sigma-Aldrich, Cat# H0135) was used for induction of  
443 airway epithelial cells.

444

445

## 446 **SARS-CoV-2 preparation and titration**

447 An Omicron subvariants (BA.1 lineage, strain TY38-873, GISAID ID:  
448 EPI\_ISL\_7418017; BA.2 lineage, strain TY40-385, GISAID ID:  
449 EPI\_ISL\_9595859; BA.5 lineage, strain TKYS14631, GISAID ID:  
450 EPI\_ISL\_12812500)<sup>14</sup> was obtained from the National Institute of Infectious  
451 Diseases (BA.1 and BA.2) and Tokyo Metropolitan Institute of Public Health,  
452 Japan. An early pandemic D614G-bearing isolate (B.1.1 lineage, strain  
453 TKYE610670; GISAID ID: EPI\_ISL\_479681) was used in the previous study<sup>10</sup>.  
454 Virus preparation and titration was performed as previously described<sup>10,12,29</sup>. To  
455 prepare the working virus stock, 20 µl of the seed virus was inoculated into  
456 VeroE6/TMPRSS2 cells (5 × 10<sup>6</sup> cells in a T-75 flask). One hour after infection,  
457 the culture medium was replaced with DMEM (low glucose) (Wako, Cat#  
458 041-29775) containing 2% FBS and 1% PS. At 3 d.p.i., the culture medium was  
459 harvested and centrifuged, and the supernatants were collected as the working  
460 virus stock. The viral genome sequences of working viruses were verified as  
461 described below.

462 The titer of the prepared working virus was measured as the 50% tissue culture  
463 infectious dose (TCID<sub>50</sub>). Briefly, one day before infection, VeroE6/TMPRSS2  
464 cells (10,000 cells) were seeded into a 96-well plate. Serially diluted virus stocks  
465 were inoculated into the cells and incubated at 37°C for 4 d. The cells were  
466 observed under microscopy to judge the CPE appearance. The value of  
467 TCID<sub>50</sub>/ml was calculated with the Reed–Muench method<sup>30</sup>.

468

## 469 **SARS-CoV-2 infection**

470 One day before infection, VeroE6/TMPRSS2 cells and Calu-3 cells were seeded  
471 into a 12-well plate. SARS-CoV-2 was inoculated as a m.o.i. = 0.1 and incubated  
472 at 37°C for 1 h. The infected cells were washed, and 1 ml of culture medium was  
473 added. The culture supernatant (100 µl) and cells were collected at the indicated  
474 time points and purified RNA for RT–qPCR to quantify the viral RNA copy  
475 number (see below). To monitor the syncytium formation in infected cell culture,  
476 bright-field photos were obtained using an Elipse Ts2 microscope (Nikon).  
477 The infection experiment human iPSC-derived alveolar epithelial cells was  
478 performed as previously described<sup>10</sup>. Briefly, the working viruses were diluted  
479 with Opti-MEM (Thermo Fisher Scientific, Cat# 11058021). The diluted viruses  
480 (1,000 TCID<sub>50</sub> in 100 µl) were inoculated onto the apical side of the culture and  
481 incubated at 37°C for 1 h. The inoculated viruses were removed and washed  
482 twice with Opti-MEM. To harvest the viruses on the apical side of the culture,  
483 100 µl Opti-MEM was applied onto the apical side of the culture and incubated at  
484 37°C for 10 min. The Opti-MEM applied was harvested and used for RT–qPCR  
485 to quantify the viral RNA copy number (see below).

486

# **487 Syncytia formation assay**

488 A equal amount of VeroE6/TMPRSS2 cells expressing either EGFP or mCheery  
489 ware seeded into the 12-well plate once day before SARS-CoV-2 infection. The  
490 infection was conducted as described above and captured the image at 48 h p.i.  
491 Florescent images were acquired with Eclipse Ti2 (Nikon, Tokyo, Japan)  
492 microscope, equipped with a PlanApo 20x/0.8 objective lens, a TI2-CTRE  
493 microscope controller (Nikon), a TI2-S-SE-E motorized stage (Nikon), and an  
494 X-Cite turbo system (Excelitas Technologies). The detectors used in this study  
495 was a PRIME95B scientific complementary metal-oxide semiconductor  
496 (sCMOS) camera (Oxford Instruments). The sets of excitation and emission  
497 filters and dichroic mirrors adopted for this observation included GFP HQ (Nikon)  
498 for EGFP, Cy3 HQ (Nikon) for mCherry.

499

# **500 Immunoblotting**

501 Cells lysed on ice in lysis buffer (20 mM Tris-HCl [pH 7.4], 135 mM NaCl, 1%  
502 Triton-X 100, 10% glycerol) supplemented with a protease inhibitor cocktail,  
503 cOmplete mini (MilliporeSigma), were boiled in loading buffer and subjected to  
504 5%–20% gradient SDS-PAGE. The proteins were transferred to polyvinylidene  
505 difluoride membranes (MilliporeSigma) and incubated with the  
506 anti-SARAS-CoV-2 S antibody (1:5,000 dilution; GeneTex) or anti-N antibody  
507 (1:5,000 dilution; Sino Biological). The immune complexes were visualized with  
508 SuperSignal West Femto substrate (Thermo Fisher Scientific). The signals were  
509 detected by use of a WSE-LuminoGraph I (ATTO) and ImageSaver6 (ATTO).

510

# **511 Airway-on-a-chip**

512 Human lung microvascular endothelial cells (HMVEC-L) were obtained from  
513 Lonza and cultured with the EGM-2-MV medium (Lonza). To prepare the  
514 airway-on-a-chip, first, the bottom channel of a polydimethylsiloxane (PDMS)  
515 device was pre-coated with fibronectin (3 µg/ml, Sigma). The microfluidic device  
516 was generated according to our previous report<sup>31</sup>. HMVEC-L were suspended at  
517  $5 \times 10^6$  cells/mL in the EGM2-MV medium. Then, 10 µl suspension medium was  
518 injected into the fibronectin-coated bottom channel of the PDMS device. Then,  
519 the PDMS device was turned upside down and incubated for 1 h. After 1 h, the  
520 device was turned over, and EGM2-MV medium was added into the bottom  
521 channel. After 4 days, human airway organoids (AO) were dissociated and  
522 seeded into the top channel. The AO was generated according to our previous  
523 report<sup>32</sup>. AO were dissociated into single cells and then suspended at  $5 \times 10^6$   
524 cells/mL in AO differentiation medium. Ten µL suspension medium was injected  
525 into the top channel. After 1 h, AO differentiation medium was added to the top



channel. The cells were cultured under a humidified atmosphere with 5% CO<sub>2</sub> at 37 °C.

528

## 529 **Electron Microscopy**

EM analyses were performed as previously described<sup>33</sup>. Briefly, cells were fixed with 2% glutaraldehyde (Electron Microscopy Sciences) in HEPES buffer (pH 7.4; 30 mM HEPES, 0.1 M NaCl and 2 mM CaCl<sub>2</sub>) and 2% osmium tetroxide (TAAB) in 0.1 M imidazole (pH 7.4). After dehydration and substitution, the cells were embedded in Araldite-Epon (Electron Microscopy Sciences). Ultrathin sections (~70 nm) were mounted on formvar-coated copper grids (SP 3 slit mesh, Nisshin EM), and the sections were imaged with a transmission electron microscope (JEM-1400, JEOL) operating at 80 kV.

538

## 539 **RT-qPCR**

RT-qPCR was performed as previously described<sup>10,12,29</sup>. Briefly, 5 µl of culture supernatant was mixed with 5 µl of 2 × RNA lysis buffer [2% Triton X-100, 50 mM KCl, 100 mM Tris-HCl (pH 7.4), 40% glycerol, 0.8 U/µl recombinant RNase inhibitor (Takara-Bio)] and incubated at room temperature for 10 min. RNase-free water (90 µl) was added, and the diluted sample (2.5 µl) was used as the template for real-time RT-PCR performed according to the manufacturer's protocol using the One Step TB Green PrimeScript PLUS RT-PCR kit (Takara-Bio) and the following primers: Forward *N*, 5'-AGC CTC TTC TCG TTC CTC ATC AC-3'; and Reverse *N*, 5'-CCG CCA TTG CCA GCC ATT C-3'. The viral RNA copy number was standardized with a SARS-CoV-2 direct detection RT-qPCR kit (Takara, Cat# RC300A). Fluorescent signals were acquired using QuantStudio Real-Time PCR system (Thermo Fisher Scientific), CFX Connect Real-Time PCR Detection system (Bio-Rad), Eco Real-Time PCR System (Illumina), qTOWER3 G Real-Time System (Analytik Jena) or 7500 Real-Time PCR System (Thermo Fisher Scientific).

To evaluate Inflammation levels evoked by viral infection in hamsters, 500 µg of the lung RNA were subjected to synthesize cDNA using SuperScript IV VILO Master Mix. The resulting cDNA was used to quantify host genes<sup>34</sup> (see **Supplementary Table 1**) with a Power SYBER Green Master Mix (Thermo Fisher Scientific) and QuantStudio Real-time PCR System (Thermo Fisher Scientific).

561

## 562 **Plasmid construction**

The cDNA clones of EGFP and mCherry were inserted between the *Xho*I and *Xba*I sites of the lentiviral vector pCSII-EF-RfA<sup>35</sup> by using the Infusion technique, and the resulting plasmids were designated pCSII-EF-EGFP, pCSII-EF-mCherry respectively.

567

568

## 569 **Animal experiments**

570 Syrian hamsters (male, 4 weeks old) were purchased from Japan SLC Inc.  
 571 (Shizuoka, Japan). Baseline body weights, respiratory parameters, and SpO<sub>2</sub>  
 572 were measured before infection. For the virus infection experiments, hamsters  
 573 were euthanized by intramuscular injection of a mixture of 0.15 mg/kg  
 574 medetomidine hydrochloride (Domitor<sup>®</sup>, Nippon Zenyaku Kogyo), 2.0 mg/kg  
 575 midazolam (Dormicum<sup>®</sup>, FUJIFILM Wako Chemicals) and 2.5 mg/kg  
 576 butorphanol (Vetorphale<sup>®</sup>, Meiji Seika Pharma) or 0.15 mg/kg medetomidine  
 577 hydrochloride, 2.0 mg/kg alphaxalone (Alfaxan<sup>®</sup>, Jurox) and 2.5 mg/kg  
 578 butorphanol. The B.1.1 virus, Omicron subvariants (5 x 1,000 TCID<sub>50</sub> in 100 µl),  
 579 or saline (100 µl) were intranasally inoculated under anesthesia. Oral swabs  
 580 were collected at indicated timepoints. Body weight was recorded daily by day 7  
 581 p.i., and days 10 and 14 p.i. Enhanced pause (Penh, see below), the ratio of  
 582 time to peak expiratory flow relative to the total expiratory time (Rpef, see  
 583 below), and subcutaneous oxygen saturation (SpO<sub>2</sub>, see below) were monitored  
 584 on days 1, 3, 5, and 7 p.i. Lung tissues were anatomically collected on days 2  
 585 and 5 p.i. Viral RNA load in the oral swabs and respiratory tissues were  
 586 determined by RT-qPCR. Viral titers in the lung periphery were determined by a  
 587 TCID<sub>50</sub>. These tissues were also used for histopathological and IHC analyses  
 588 (see below).

589

## 590 **Lung function test**

591 Respiratory parameters (Penh and Rpef) were measured by using a whole-body  
 592 plethysmography system (DSI) according to the manufacturer's instructions. In  
 593 brief, a hamster was placed in an unrestrained plethysmography chamber and  
 594 allowed to acclimatize for 30 s, then, data were acquired over a 2.5-min period by  
 595 using FinePointe Station and Review softwares v2.9.2.12849 (STARR). The  
 596 state of oxygenation was examined by measuring SpO<sub>2</sub> using pulse oximeter,  
 597 MouseOx PLUS (STARR). SpO<sub>2</sub> was measured by attaching a measuring chip  
 598 to the neck of hamsters sedated by 0.25 mg/kg medetomidine hydrochloride.

599

## 600 **H&E staining**

601 H&E staining was performed as described in the previous study<sup>10</sup>. Briefly,  
 602 excised animal tissues were fixed with 10% formalin neutral buffer solution and  
 603 processed for paraffin embedding. The paraffin blocks were sectioned with 3  
 604 µm-thickness and then mounted on silane-coated glass slides (MAS-GP,  
 605 Matsunami). H&E staining was performed according to a standard protocol.

606

## 607 **IHC**

IHC was performed using an Autostainer Link 48 (Dako). The deparaffinized sections were exposed to EnVision FLEX target retrieval solution high pH (Agilent, Cat# K8004) for 20 m at 97°C to activate, and mouse anti-SARS-CoV-2 N monoclonal antibody (R&D systems, Clone 1035111, Cat# MAB10474-SP, 1:400) was used as a primary antibody. The sections were sensitized using EnVision FLEX (Agilent) for 15 m and visualized by peroxidase-based enzymatic reaction with 3,3'-diaminobenzidine tetrahydrochloride as substrate for 5 m. For the evaluation of the N protein positivity in the tracheae on day 2 p.i. and the lung specimens of infected hamsters on days 2 and 5 p.i. (B1.1, BA.1, BA.2, and BA.5, n = 4 each) were stained with mouse anti-SARS-CoV-2 N monoclonal antibody (R&D systems, Clone 1035111, Cat# MAB10474-SP, 1:400). The N protein positivity was evaluated by certificated pathologists as previously described<sup>9,11</sup>. Images were incorporated as virtual slide by NDP.scan software v3.2.4 (Hamamatsu Photonics). The N-protein positivity was measured as the area using Fiji software v2.2.0 (ImageJ).

#### **Histopathological scoring of lung lesion**

The inflammation area in the infected lungs was measured by the presence of the type II pneumocyte hyperplasia. Four hamsters infected with each virus were sacrificed on days 2 and 5 p.i., and all four lung lobes, including right upper (anterior/cranial), middle, lower (posterior/caudal), and accessory lobes, were sectioned along with their bronchi. The tissue sections were stained by H&E, and the digital microscopic images were incorporated into virtual slides using NDRscan3.2 software (Hamamatsu Photonics). The color of the images was decomposed by RGB in split channels using Fiji software v2.2.0.

Histopathological scoring was performed as described in the previous study. Briefly, pathological features including bronchitis or bronchiolitis, hemorrhage or congestion, alveolar damage with epithelial apoptosis and macrophage infiltration, hyperplasia of type II pneumocytes, and the area of the hyperplasia of large type II pneumocytes were evaluated by certified pathologists and the degree of these pathological findings were arbitrarily scored using four-tiered system as 0 (negative), 1 (weak), 2 (moderate), and 3 (severe). The "large type II pneumocytes" are the hyperplasia of type II pneumocytes exhibiting more than 10-μm-diameter nucleus. Total histology score is the sum of these five indices. In the representative lobe of each lung, the inflammation area with type II pneumocytes was gated by the certificated pathologists on H&E staining, and the indicated area were measured by Fiji software v2.2.0.

#### **Viral genome sequencing analysis**

The sequences of the working viruses were verified by viral RNA-sequencing analysis. Viral RNA was extracted using QIAamp viral RNA mini kit (Qiagen,

649 Cat# 52906). The sequencing library for total RNA-sequencing was prepared  
650 using NEB Next Ultra RNA Library Prep Kit for Illumina (New England Biolabs,  
651 Cat# E7530). Paired-end, 76-bp sequencing was performed using MiSeq  
652 (Illumina) with MiSeq reagent kit v3 (Illumina, Cat# MS-102-3001). Sequencing  
653 reads were trimmed using fastp v0.21.0<sup>36</sup> and subsequently mapped to the viral  
654 genome sequences of a lineage B isolate (strain Wuhan-Hu-1; GISAID ID:  
655 EPI\_ISL\_402125; GenBank accession no. NC\_045512.2) using BWA-MEM  
656 v0.7.17<sup>37</sup>. Variant calling, filtering, and annotation were performed using  
657 SAMtools v1.9<sup>38</sup> and snpEff v5.0e<sup>39</sup>. Information on the detected mutations in  
658 the working virus stocks is summarized in **Supplementary Table 2**.

659

## 660 **Statistics**

661 Viral RNA copy, body weight, Penh, Rpef, and SpO<sub>2</sub>, and inflammatory mRNA  
662 gene levels obtained from the in vivo experiments were analyzed by repeated  
663 measures analysis of variance. Inflammation measures upon infection in vivo,  
664 the mRNA of the lung hilum area on day 2 p.i. and 4 parameters (CXCL10, IL-6,  
665 ISG15, and Mx-1) were compared among Omicron subvariants using analysis of  
666 variance. Regarding Penh, Rpef and SpO<sub>2</sub>, we compared between infected and  
667 uninfected animals and calculated p-value using Dunnett adjustment. The other  
668 measurements were tested with Tukey's multiplicity correction to maintain type-I  
669 error rate to compare among infected or uninfected animals. These analyses  
670 were conducted using SAS Ver 9.4 (Cary, NC). Two-sided significance level was  
671 set to 0.05. Statistical differences between BA.5 and other variants or saline  
672 across timepoints from day 1 p.i. to day 7 p.i. were determined by multiple  
673 regression. The family-wise error rates calculated using the Holm method. The  
674 indicated analyses were performed in R v4.1.2 (<https://www.r-project.org/>).

# References

- 1 WHO. "Classification of Omicron (B.1.1.529): SARS-CoV-2 variant of concern (November 26, 2021)" [https://www.who.int/news/item/26-11-2021-classification-of-omicron-\(b.1.1.529\)-sars-cov-2-variant-of-concern](https://www.who.int/news/item/26-11-2021-classification-of-omicron-(b.1.1.529)-sars-cov-2-variant-of-concern). (2020).
- 2 Tegally, H. *et al.* Emergence of SARS-CoV-2 Omicron lineages BA.4 and BA.5 in South Africa. *Nat Med* (2022). <https://doi.org/10.1038/s41591-022-01911-2>
- 3 Kislaya, I. C., Pedro Borges, Vítor Sousa, Carlos Ferreira, Bibiana I. Fernandes, Eugénia Dias, Carlos Matias Duarte, Sílvia Almeida, José Pedro Grenho, Inês Coelho, Luís Ferreira, Rita Ferreira, Patrícia Pita Isidro, Joana Pinto, Miguel Menezes, Luís Sobral, Daniel Nunes, Alexandra Santos, Daniela Gonçalves, António Maia Vieira, Luís Gomes, João Paulo Leite, Pedro Pinto Nunes, Baltazar Machado, Ausenda Peralta-Santos, André. Vol. 2022.07.25.22277996 (medRxiv, 2022).
- 4 Cao, Y. *et al.* BA.2.12.1, BA.4 and BA.5 escape antibodies elicited by Omicron infection. *Nature* (2022). <https://doi.org/10.1038/s41586-022-04980-y>
- 5 Hachmann, N. P. *et al.* Neutralization Escape by SARS-CoV-2 Omicron Subvariants BA.2.12.1, BA.4, and BA.5. *N Engl J Med* **387**, 86-88 (2022). <https://doi.org/10.1056/NEJMc2206576>
- 6 Qu, P. *et al.* Neutralization of the SARS-CoV-2 Omicron BA.4/5 and BA.2.12.1 Subvariants. *N Engl J Med* **386**, 2526-2528 (2022). <https://doi.org/10.1056/NEJMc2206725>
- 7 Tuekprakhon, A. *et al.* Antibody escape of SARS-CoV-2 Omicron BA.4 and BA.5 from vaccine and BA.1 serum. *Cell* **185**, 2422-2433.e2413 (2022). <https://doi.org/10.1016/j.cell.2022.06.005>
- 8 Arora, P. *et al.* Augmented neutralisation resistance of emerging omicron subvariants BA.2.12.1, BA.4, and BA.5. *Lancet Infect Dis* (2022). [https://doi.org/10.1016/S1473-3099\(22\)00422-4](https://doi.org/10.1016/S1473-3099(22)00422-4)
- 9 Yamasoba, D. *et al.* Virological characteristics of the SARS-CoV-2 Omicron BA.2 spike. *Cell* (2022). <https://doi.org/10.1016/j.cell.2022.04.035>
- 10 Saito, A. *et al.* Enhanced fusogenicity and pathogenicity of SARS-CoV-2 Delta P681R mutation. *Nature* **602**, 300-306 (2022). <https://doi.org/10.1038/s41586-021-04266-9>
- 11 Suzuki, R. *et al.* Attenuated fusogenicity and pathogenicity of SARS-CoV-2 Omicron variant. *Nature* (2022).

- 716 <https://doi.org/10.1038/s41586-022-04462-1>
- 717 12 Motozono, C. *et al.* SARS-CoV-2 spike L452R variant evades cellular  
718 immunity and increases infectivity. *Cell Host Microbe* **29**, 1124-1136  
719 (2021). <https://doi.org/10.1016/j.chom.2021.06.006>
- 720 13 Kimura, I. Y., Daichi Tamura, Tomokazu Nao, Naganori Oda,  
721 Yoshitaka Mitoma Shuya Ito, Jumpei Nasser, Hesham Zahradnik,  
722 Jiri Uriu, Keiya Fujita, Shigeru Kosugi, Yusuke Wang, Lei Tsuda,  
723 Masumi Kishimoto, Mai Ito, Hayato Suzuki, Rigel Shimizu, Ryo  
724 Begum, MST Monira Yoshimatsu, Kumiko Sasaki, Jiei  
725 Sasaki-Tabata, Kaori Yamamoto, Yuki Nagamoto, Tetsuharu  
726 Kanamune, Jun Kobiyama, Kouji Asakura, Hiroyuki Nagashima,  
727 Mami Sadamasu, Kenji Yoshimura, Kazuhisa Kuramochi, Jin  
728 Schreiber, Gideon Ishii, Ken J Hashiguchi, Takao The Genotype to  
729 Phenotype Japan (G2P-Japan) Consortium, Ikeda, Terumasa Saito,  
730 Akatsuki Fukuhara, Takasuke Tanaka, Shinya Matsuno, Keita  
731 Sato, Kei. (bioRxiv 2022).
- 732 14 Miyamoto, S. *et al.* Vaccination-infection interval determines  
733 cross-neutralization potency to SARS-CoV-2 Omicron after breakthrough  
734 infection by other variants. *MedRxiv*, doi:  
735 <https://doi.org/10.1101/2021.1112.1128.21268481> (2022).
- 736 15 Matsuyama, S. *et al.* Enhanced isolation of SARS-CoV-2 by  
737 TMPRSS2-expressing cells. *Proc Natl Acad Sci U S A* **117**, 7001-7003  
738 (2020). <https://doi.org/10.1073/pnas.2002589117>
- 739 16 Eymieux, S. *et al.* Ultrastructural modifications induced by SARS-CoV-2  
740 in Vero cells: a kinetic analysis of viral factory formation, viral particle  
741 morphogenesis and virion release. *Cell Mol Life Sci* **78**, 3565-3576 (2021).  
742 <https://doi.org/10.1007/s00018-020-03745-y>
- 743 17 Walther, T. C. *et al.* RanGTP mediates nuclear pore complex assembly.  
744 *Nature* **424**, 689-694 (2003). <https://doi.org/10.1038/nature01898>
- 745 18 Cele, S. *et al.* Omicron extensively but incompletely escapes Pfizer  
746 BNT162b2 neutralization. *Nature*, doi:  
747 <https://doi.org/10.1038/d41586-41021-03824-41585> (2021).
- 748 19 Cao, Y. *et al.* Omicron escapes the majority of existing SARS-CoV-2  
749 neutralizing antibodies. *Nature*, doi:  
750 <https://doi.org/10.1038/d41586-41021-03796-41586> (2021).
- 751 20 Cameroni, E. *et al.* Broadly neutralizing antibodies overcome  
752 SARS-CoV-2 Omicron antigenic shift. *Nature*, doi:  
753 <https://doi.org/10.1038/d41586-41021-03825-41584> (2021).
- 754 21 Planas, D. *et al.* Considerable escape of SARS-CoV-2 Omicron to  
755 antibody neutralization. *Nature*, doi:  
756 <https://doi.org/10.1038/d41586-41021-03827-41582> (2021).



- 757 22 Meng, B. *et al.* SARS-CoV-2 Omicron spike mediated immune escape,  
758 infectivity and cell-cell fusion. *BioRxiv*, doi:  
759 <https://doi.org/10.1101/2021.1112.1103.471045> (2021).
- 760 23 Liu, L. *et al.* Striking antibody evasion manifested by the Omicron variant  
761 of SARS-CoV-2. *Nature*, doi:  
762 <https://doi.org/10.1038/d41586-41021-03826-41583> (2021).
- 763 24 Kawaoka, Y. U., Ryuta Halfmann, Peter Iida, Shun Yamayoshi,  
764 Seiya Furusawa, Yuri Kiso, Maki Ito, Mutsumi Iwatsuki-Horimoto,  
765 Kiyoko Mine, Sohtaro Kuroda, Makoto Maemura, Tadashi Sakai,  
766 Yuko Ueki, Hiroshi Li, Rong Liu, Yanan Larson, Deanna Fukushi,  
767 Shuetsu Watanabe, Shinji Maeda, Ken Pekosz, Andrew Kandeil,  
768 Ahmed Webby, Richard Wang, Zhongde Imai, Masaki Suzuki,  
769 Tadaki. Vol. <https://www.researchsquare.com/article/rs-1820048/v1>  
770 (Research Square, 2022).
- 771 25 Reuschl, A.-K. T., Lucy G. Whelan, Matthew V.X. Mesner, Dejan  
772 Ragazzini, Roberta Dowgier, Giulia Bogoda, Nathasha Turner, Jane  
773 L. E. Furnon, Wilhelm Cowton, Vanessa M. de Lorenzo, Giuditta  
774 Bonfanti, Paola Palmarini, Massimo Patel, Arvind H. Jolly, Clare  
775 Towers, Greg. J. Vol. 2022.07.12.499603 (bioRxiv 2022).
- 776 26 Yamamoto, Y. *et al.* Long-term expansion of alveolar stem cells derived  
777 from human iPS cells in organoids. *Nat Methods* **14**, 1097-1106 (2017).  
778 <https://doi.org/10.1038/nmeth.4448>
- 779 27 Konishi, S. *et al.* Directed Induction of Functional Multi-ciliated Cells in  
780 Proximal Airway Epithelial Spheroids from Human Pluripotent Stem Cells.  
781 *Stem Cell Reports* **6**, 18-25 (2016).  
782 <https://doi.org/10.1016/j.stemcr.2015.11.010>
- 783 28 Gotoh, S. *et al.* Generation of alveolar epithelial spheroids via isolated  
784 progenitor cells from human pluripotent stem cells. *Stem Cell Reports* **3**,  
785 394-403 (2014). <https://doi.org/10.1016/j.stemcr.2014.07.005>
- 786 29 Saito, A. *et al.* Enhanced fusogenicity and pathogenicity of SARS-CoV-2  
787 Delta P681R mutation. *Nature* (2021).  
788 <https://doi.org/10.1038/s41586-021-04266-9>
- 789 30 Reed, L. J. & Muench, H. A Simple Method of Estimating Fifty Percent  
790 Endpoints. *Am J Hygiene* **27**, 493-497 (1938).
- 791 31 Deguchi, S. *et al.* Usability of Polydimethylsiloxane-Based Microfluidic  
792 Devices in Pharmaceutical Research Using Human Hepatocytes. *ACS*  
793 *Biomater Sci Eng* **7**, 3648-3657 (2021).  
794 <https://doi.org/10.1021/acsbiomaterials.1c00642>
- 795 32 Sano, E. *et al.* Cell response analysis in SARS-CoV-2 infected bronchial  
796 organoids. *Commun Biol* **5**, 516 (2022).  
797 <https://doi.org/10.1038/s42003-022-03499-2>

- 798 33 Kamasaki, T. *et al.* FBP17-mediated finger-like membrane protrusions in  
799 cell competition between normal and RasV12-transformed cells. *iScience*  
800 **24**, 102994 (2021). <https://doi.org/10.1016/j.isci.2021.102994>
- 801 34 Bessi re, P. *et al.* Intranasal type I interferon treatment is beneficial only  
802 when administered before clinical signs onset in the SARS-CoV-2  
803 hamster model. *PLoS Pathog* **17**, e1009427 (2021).  
804 <https://doi.org/10.1371/journal.ppat.1009427>
- 805 35 Fukuhara, T. *et al.* Amphipathic alpha-helices in apolipoproteins are  
806 crucial to the formation of infectious hepatitis C virus particles. *PLoS*  
807 *Pathog* **10**, e1004534 (2014).  
808 <https://doi.org/10.1371/journal.ppat.1004534>
- 809 36 Chen, S., Zhou, Y., Chen, Y. & Gu, J. fastp: an ultra-fast all-in-one  
810 FASTQ preprocessor. *Bioinformatics* **34**, i884-i890 (2018).  
811 <https://doi.org/10.1093/bioinformatics/bty560>
- 812 37 Li, H. & Durbin, R. Fast and accurate long-read alignment with  
813 Burrows-Wheeler transform. *Bioinformatics* **26**, 589-595 (2010).  
814 <https://doi.org/10.1093/bioinformatics/btp698>
- 815 38 Danecek, P. *et al.* Twelve years of SAMtools and BCFtools. *Gigascience*  
816 **10** (2021). <https://doi.org/10.1093/gigascience/giab008>
- 817 39 Cingolani, P. *et al.* A program for annotating and predicting the effects of  
818 single nucleotide polymorphisms, SnpEff: SNPs in the genome of  
819 *Drosophila melanogaster* strain w1118; iso-2; iso-3. *Fly (Austin)* **6**, 80-92  
820 (2012). <https://doi.org/10.4161/fly.19695>

821  
822

823 **Supplementary Table 1. Primers used for quantifying the host genes of**  
824 **hamster upon infection with the SARS-CoV-2 variants in this study.**

825

826 **Supplementary Table 2. Mutations in Omicron subvariants.**

827

828 **Supplementary Fig. 1. *In vivo* dynamics of Omicron subvariants in related**  
829 **to Fig.2.** Dynamics of of body weight (A), Penh (B), Rpef (C), and SpO2 (D)  
830 within Omicron subvariants by days 7 p.i were shown. Saline injection was  
831 served as a control in this study.

832

833 **Supplementary Fig. 2. Virological features of Omicron subvariants *in vivo***  
834 **in the trachea related to Fig. 3.** Percentage of N-positive cells in the upper part  
835 of the trachea from the oral entrance at the vertical levels of thyroid cartilage on  
836 day 2 p.i. was shown. Scale bars, 1 mm.

837

838 **Supplementary Fig. 3. Virological features of Omicron subvariants *in vivo***  
839 **in the lung related to Fig. 3.** Percentage of N-positive cells in whole lung lobes  
840 on day 2 p.i. was shown. Scale bars, 5 mm.

841

842 **Supplementary Fig. 4. Pathological features of Omicron subvariants *in***  
843 ***vivo* related to Fig. 4.** Section of all four lung lobes on day 5 p.i. H&E staining  
844 and the inflammatory area with type II pneumocytes are shown. The  
845 inflammatory area is colored in red. The number in the panel indicates the  
846 percentage of the section represented by the indicated area. Scale bars,5 mm.

847

## 848 **Author Contributions**

849 Tomokazu Tamura, Daichi Yamasoba, Tomoko Kamasaki, Rina Hashimoto,  
850 Yoichiro Fujioka, Rigel Suzuki, Hayato Ito, Izumi Kimura, performed cell culture  
851 experiments.

852 Tomokazu Tamura, Naganori Nao, Rigel Suzuki, Hayato Ito Mai Kishimoto,  
853 Hirofumi Sawa, Kumiko Yoshimatsu performed animal experiments.

854 Yoshitaka Oda, Lei Wang, Masumi Tsuda, Shinya Tanaka performed  
855 histopathological analysis.

856 Daichi Yamasoba, Izumi Kimura, and Jumpei Ito performed viral genome  
857 sequencing analysis.

858 Jumpei Ito, Isao Yokota performed statistical, modelling, and bioinformatics  
859 analyses.

860 Keita Matsuno, Kazuo Takayama, Kei Sato, Takasuke Fukuhara, designed the  
861 experiments and interpreted the results.

862 Tomokazu Tamura, Takasuke Fukuhara wrote the original manuscript.

863 All authors reviewed and proofread the manuscript.

864 The Genotype to Phenotype Japan (G2P-Japan) Consortium contributed to the  
865 project administration.

866

## 867 **Conflict of interest**

868 The authors declare that no competing interests exist.

869

## 870 **Acknowledgments**

871 We would like to thank all members belonging to The Genotype to Phenotype  
872 Japan (G2P-Japan) Consortium. We thank the National Institute for Infectious  
873 Diseases, Japan, for providing BA.1 and BA.2 isolates, and Tokyo Metropolitan  
874 Institute of Public Health for providing a BA.5 isolate.

875 This study was supported in part by AMED Research Program on Emerging and  
876 Re-emerging Infectious Diseases (JP20fk0108401, to Takasuke Fukuhara;  
877 JP20fk010847, to Takasuke Fukuhara; JP21fk0108617 to Takasuke Fukuhara;  
878 JP20fk0108146, to Kei Sato; JP20fk0108451, to G2P-Japan Consortium, Keita  
879 Matsuno, Kei Sato, and Takasuke Fukuhara; JP21fk0108494 to G2P-Japan  
880 Consortium, Keita Matsuno, Shinya Tanaka, Kei Sato and Takasuke Fukuhara);  
881 AMED Program on R&D of new generation vaccine including new modality  
882 application (JP223fa727002, to Kei Sato); AMED Research Program on  
883 HIV/AIDS (21fk0410039, to Kei Sato); AMED Japan Program for Infectious  
884 Diseases Research and Infrastructure (JP22wm0125008, to Hirofumi Sawa and  
885 JP21wm0225003, to Hirofumi Sawa); AMED Research Program on infectious  
886 disease drug development (22gm1610005h0002, to Kazuo Takayama); JST  
887 CREST (JPMJCR20H4, to Kei Sato); JSPS KAKENHI Grant-in-Aid for Scientific  
888 Research B (21H02736, to Takasuke Fukuhara); JSPS Core-to-Core Program

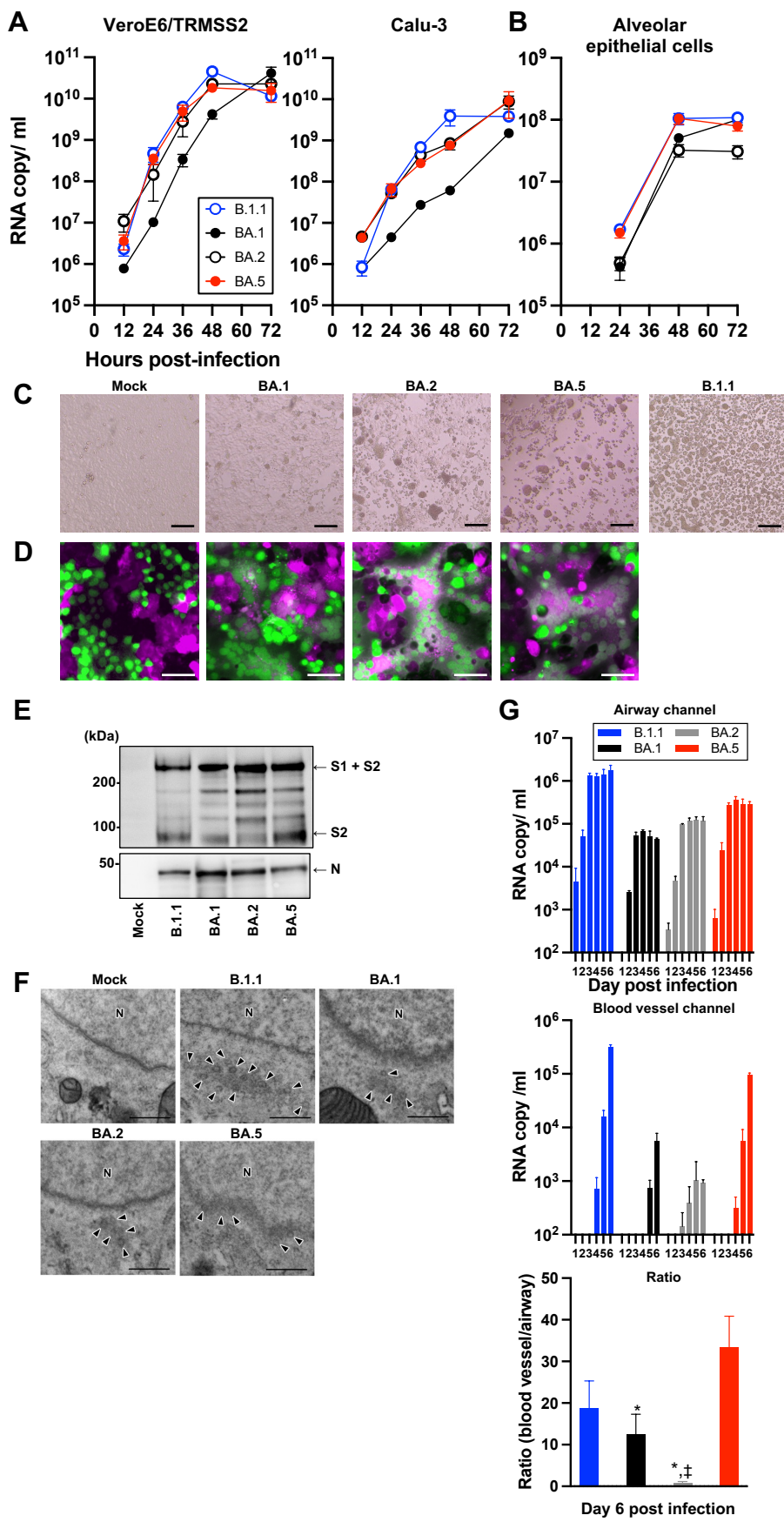
(A. Advanced Research Networks) (JPJSCCA20190008, to Kei Sato);  
World-leading Innovative and Smart Education (WISE) Program 1801 from the  
Ministry of Education, Culture, Sports, Science and Technology (MEXT) (to  
Naganori Nao); The Tokyo Biochemical Research Foundation (to Kei Sato).

#### **Data availability**

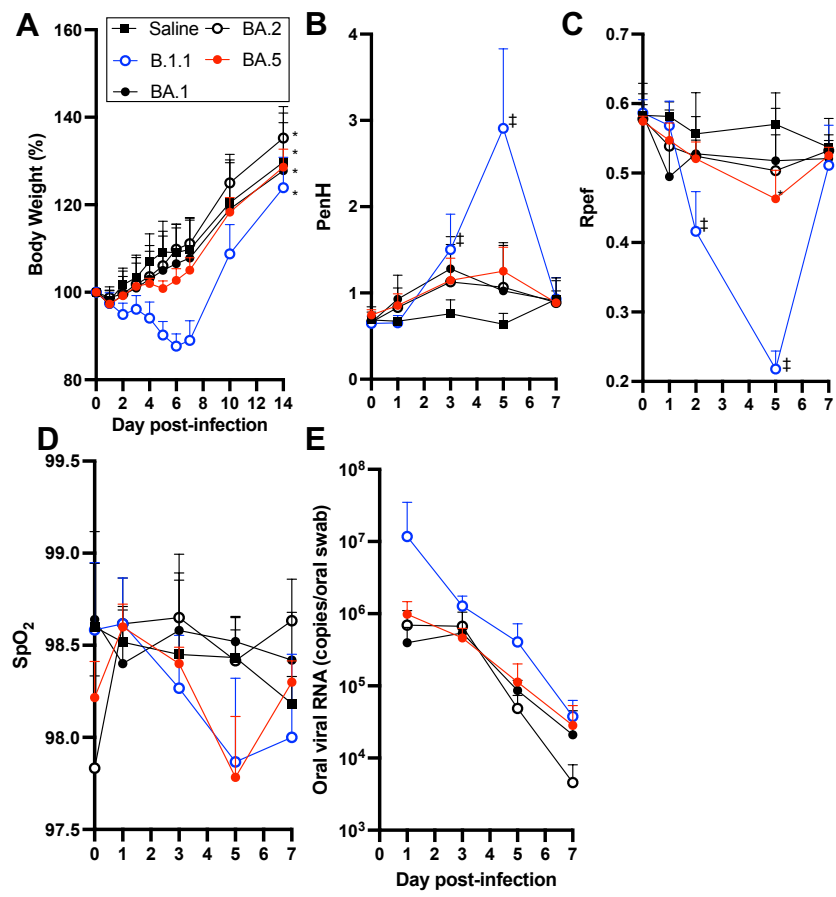
The accession numbers of viral sequences used in this study are listed in  
Method section.

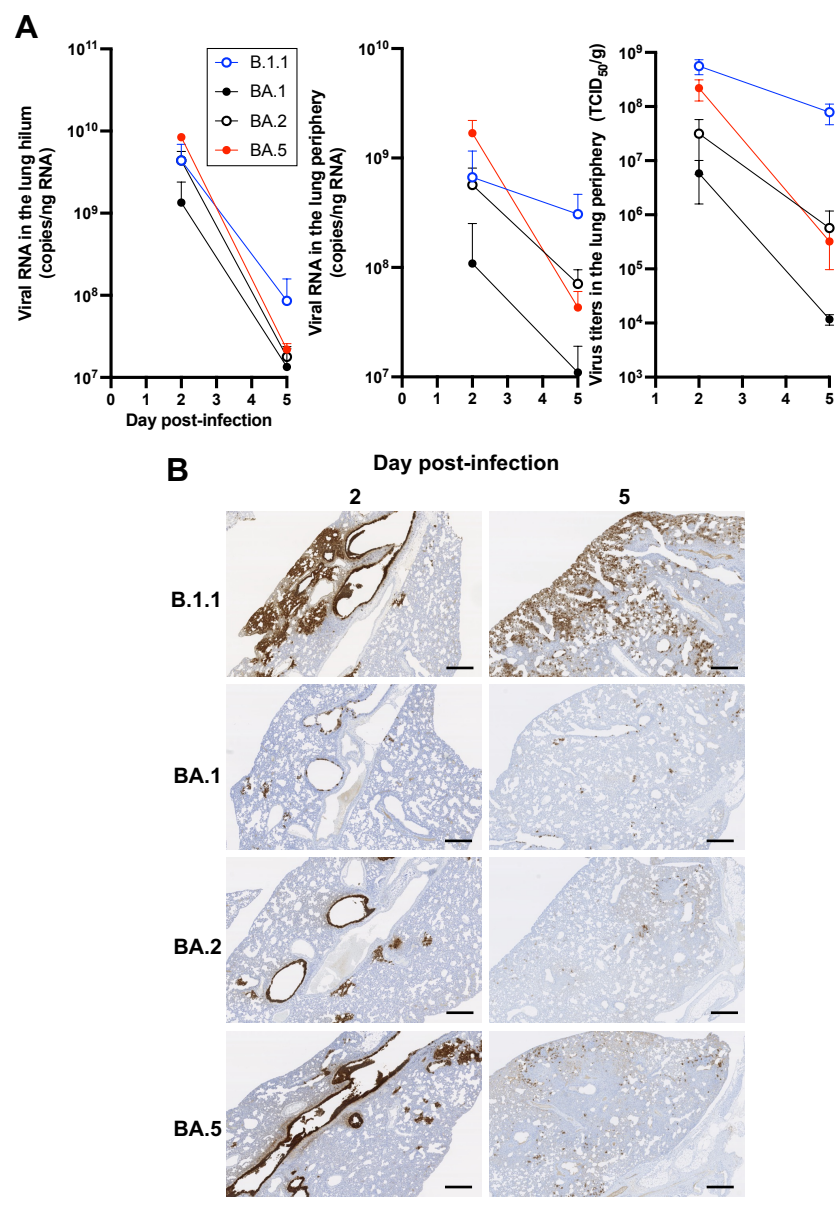
#### **Consortia**

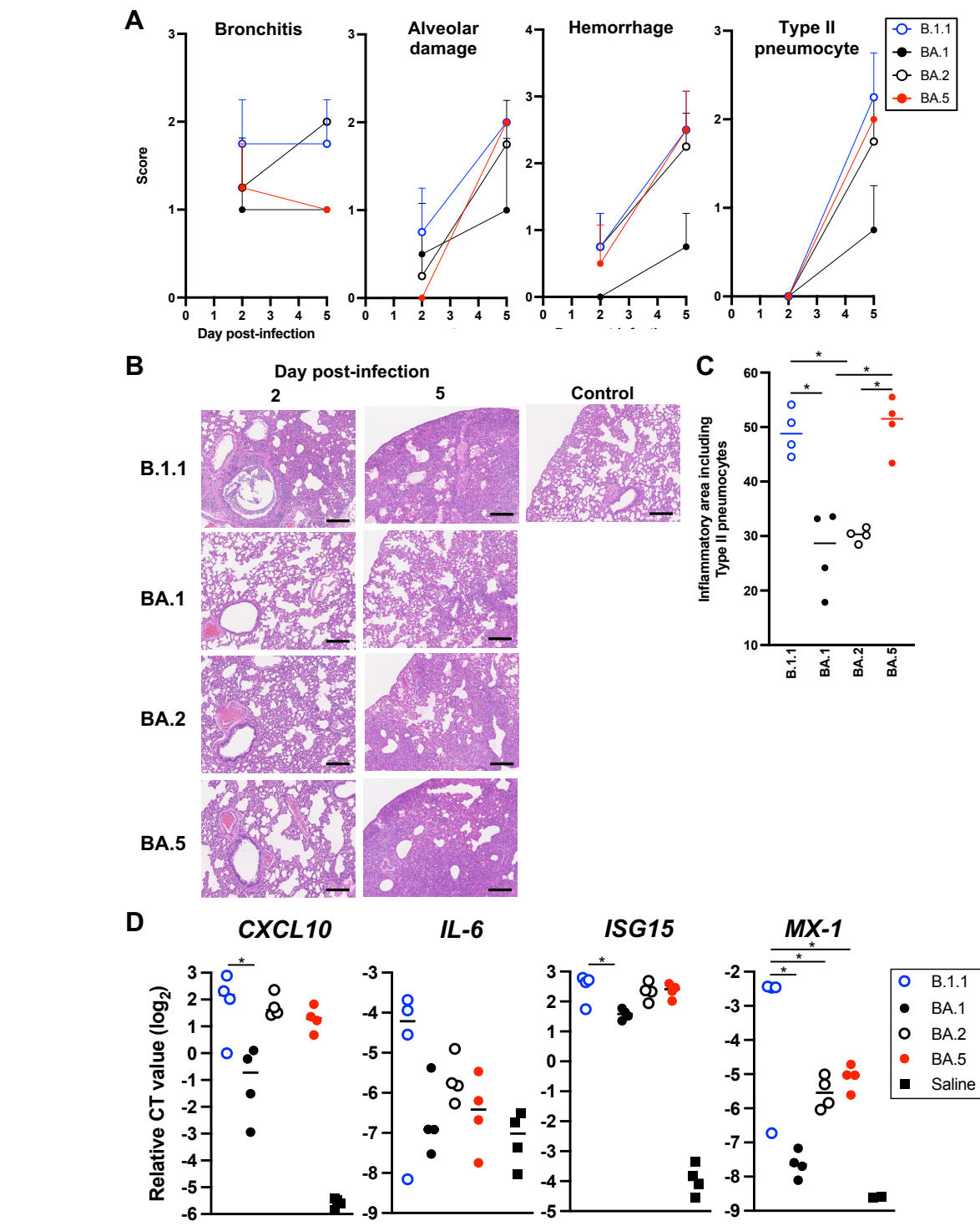
Marie Kato, Zannatul Ferdous, Hiromi Mouri, Kenji Shishido, Naoko Misawa,  
Keiya Uriu, Yusuke Kosugi, Shigeru Fujita, Mai Suganami, Mika Chiba, Ryo  
Yoshimura, So Nakagawa, Jiaqi Wu, Akifumi Takaori-Kondo, Kotaro Shirakawa,  
Kayoko Nagata, Yasuhiro Kazuma, Ryosuke Nomura, Yoshihito Horisawa,  
Yusuke Tashiro, Yugo Kawai, Takashi Irie, Ryoko Kawabata, Terumasa Ikeda,  
Hesham Nasser, Ryo Shimizu, MST Monira Begum, Otowa Takahashi, Kimiko  
Ichihara, Takamasa Ueno, Chihiro Motozono, Mako Toyoda, Akatsuki Saito,  
Yuri L. Tanaka, Erika P. Butlertanaka, Maya Shofa, Takao Hashiguchi, Teteki  
Suzuki, Kanako Kimura, Jiei Sasaki, Yukari Nakajima, Kaori Tabata



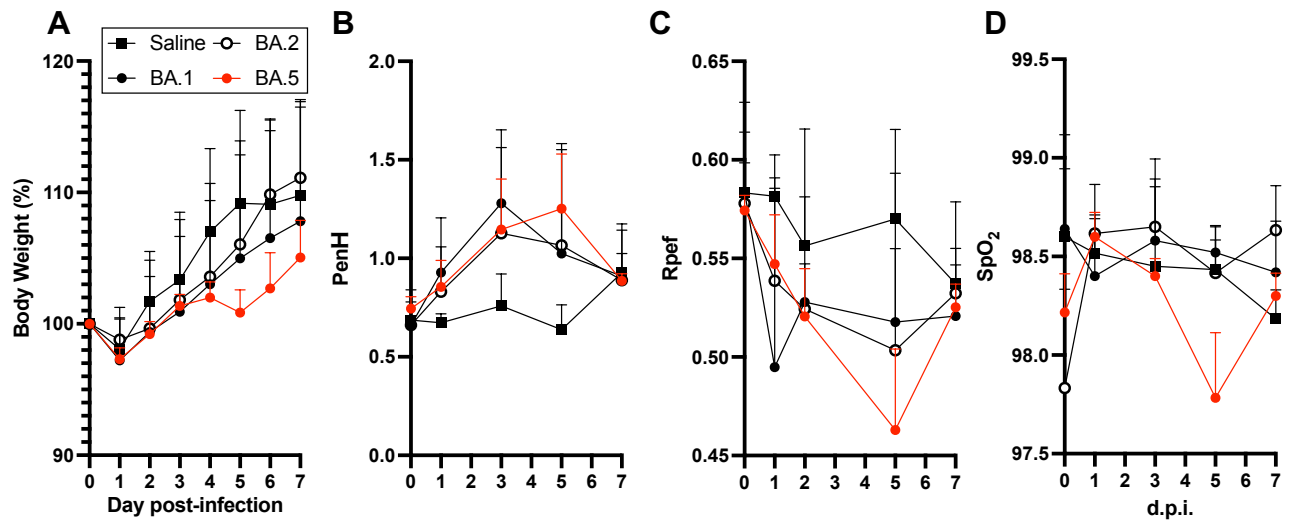




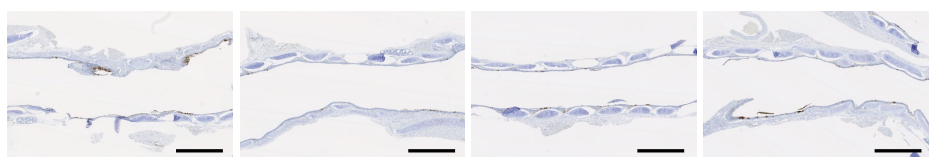




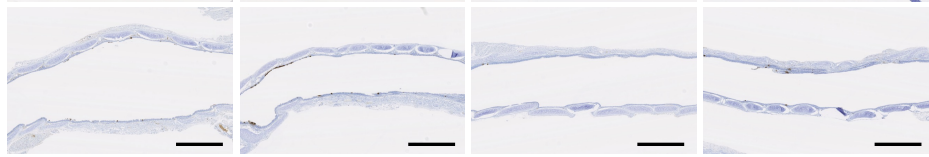
Tamura et al. Supplementary Fig. 1



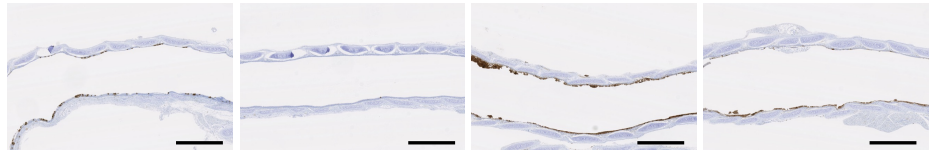
**B.1.1**



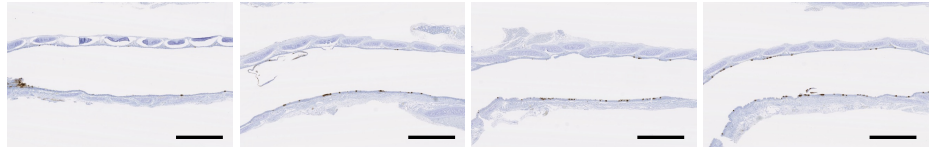
**BA.1**



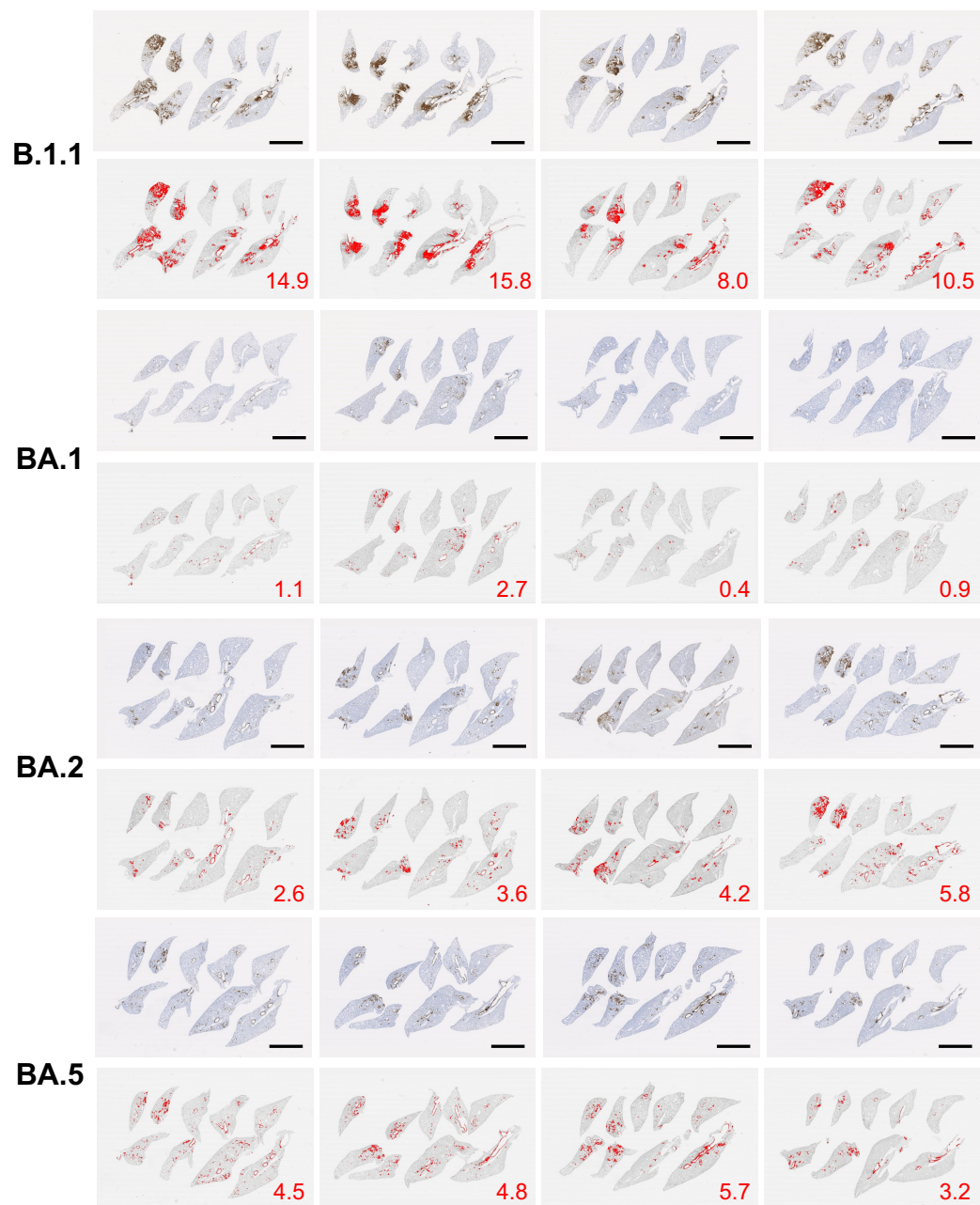
**BA.2**



**BA.5**



**Tamura et al. Supplementary Fig. 3**





**Tamura et al. Supplementary Fig. 4**

